NATIONAL UNIVERSITY OF SCIENCE AND TECHNOLOGY POLITEHNICA BUCHAREST

FACULTY OF CHEMICAL ENGINEERING AND BIOTECHNOLOGY

Multifunctionality in ferroic perovskite systems

~Phd Thesis Abstract~

Scientific advisor:

Prof.dr.eng. Adelina-Carmen Ianculescu

Phd Student:

Elena Mirabela Soare

Bucharest

2025

Introduction

One of the most suitable environmentally friendly perovskites turned out to be barium titanate ($BaTiO_3$, BT), a leading exponent of ferroelectric materials. Due to their numerous, unique and versatile characteristics, such as high permittivity, high values of pyro- and piezoelectric coefficients, ferroelectric switching, PTCR effect, large electro-optic coefficient, $BaTiO_3$-based (BT) materials have direct applications as passive elements in electronic circuits, multilayer ceramic capacitors (MLCCs), memory elements, field effect devices (FeT), pyroelectric detectors, piezoelectric actuators, thermistors, sensors, transducers, electro-optic modulators and photonic devices, etc [1-15].In recent years, intensive research and development efforts have been dedicated to study and exploit some $BaTiO_3$-based systems for tunable high-frequency devices as phase shifters, filters, antennas, microwave circuits for mobile telephony and, in general, in satellite communications [16-18]. The revival of the interest in $BaTiO_3$ materials is also related to some newly discovered characteristics as high energy density and energy efficiency, which makes them promising candidates for energy storage systems [19-22]. For each kind of purpose, specific requirements are desired. For example, energy storage applications demand for materials with high permittivity, low losses, moderate polarization and high breakdown field [19-22], while microwave devices require dielectrics with high electric-field tunability ($n = \varepsilon(E)/\varepsilon(0) \geq 1.5$), moderate permittivity below 1000 and low dielectric losses (below 3%) [23, 24]. All of these requests can occasionally be incompatible with one another, and there is a strong interest to customize the electrical characteristics by discovering new materials, material combinations, or processing parameters to provide nano/microstructural control.

The present tendency of both miniaturization and increasing degree of integration in electronic devices, where the goal is to achieve the best possible functional properties in the smallest possible volume, requires manufacturing products with confined geometry, involving nano-sized entities/architectures or nanostructuring.

1. Influence of Hf content in $BaTi_{1-x}Hf_xO_3$ systems prepared by the modified Pechini method

Composition, phase purity and crystal structure

The room-temperature XRD patterns of $BaTi_{1-x}Hf_xO_3$ nanopowders displayed in Fig. 1(a) show the presence of the well-crystallized perovskite phase, without any detectable Ba- or Ti-rich secondary phases [25]. Increasing hafnium proportion determines the shift of the XRD peaks towards lower values of the diffraction angle 2θ, due to the increase of the unit cell volume. This evolution and the perovskite phase's purity are clear proofs that Hf^{4+} is completely incorporated onto Ti sites in the BT lattice to create homogeneous BTH solid solutions. The crystallinity degree of all the four BTH powders exceeds 90%. As demonstrated by the detail of the region corresponding to the diffraction angles 2θ = 44.5-46.5° in Fig. 1(b), the symmetric appearance of their profiles and the lack of any splitting of the (200) reflections seem to indicate a pseudo-cubic structure.

Using the Rietveld refinement, the best fits were obtained when considering a mixture of tetragonal and cubic phases for all the BTH powders under investigation. To fit the XRD data as accurately as possible, a number of variants were considered, taking into account the complex distortions found in nanosized BT-based systems [26, 27-32]. These included the single-phase model (cubic C for all the four powders, tetragonal T and orthorhombic O for BTH powders with x = 0, 0.05, 0.10 and rhombohedral R for x = 0.10, 0.20), the di-phase model (T+C for all the samples, T+R and R+C for x = 0.10 and x = 0.20), as well as tri-phase model (T+R+C for x = 0.20).

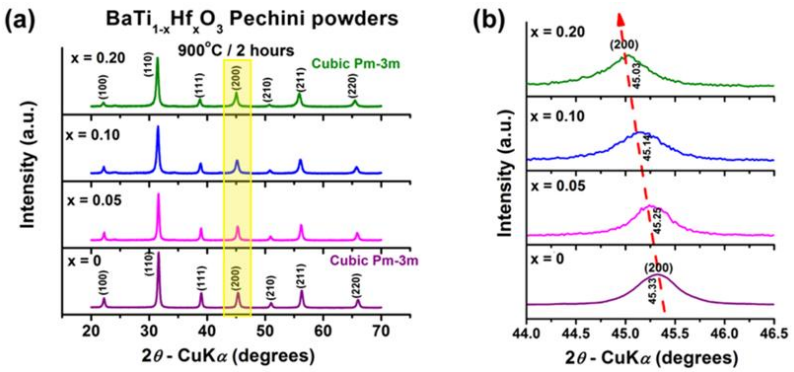


Fig. 1. (a) Room-temperature X-ray diffraction patterns of $BaTi_{1-x}Hf_xO_3$ nanopowders prepared by the modified Pechini method and annealed at 900°C for 2 hours and (b) detail (the yellowish rectangle of Fig. 1(a)) of the region corresponding to the diffraction angles 2θ = 44.5 - 46.5° [25].

Morphology

Bright-field TEM images presented in Fig. 2(a)-(d) show the morphology of the investigated BTH powders. All the compositions consist of particles with sizes in the nanometre range. Similar to the mean crystallite size, it was found that the mean particle size <*d*> dropped as the solute content increased from 39.8 nm for the undoped BT powder (inset of Fig. 2(a)) down to 15.3 nm for the powder with the highest Hf content, *i.e.* BTH20 (inset of Fig. 2(d)). This trend suggests the inhibiting effect of the Hf solute on the particles coarsening. Comparing the values of the mean crystallite size calculated from the XRD data with the values of mean particle size estimated from the TEM investigations, one can conclude that the nanoparticles are predominantly single crystals. The equiaxed nanoparticles exhibit mostly polyhedral shapes with well-defined planar faces and edges and somewhat rounded corners. Some ultrafine rounded or almost spherical particles can also be noticed. Their size distributions are uni-modal, as indicated by the histograms presented as insets in the top-right corners of Fig. 2 (a)-(d).

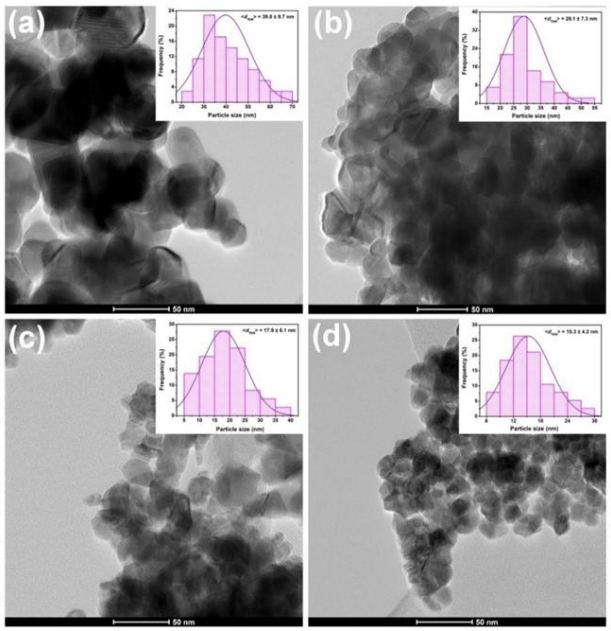


Fig. 2.(a)-(d) TEM images of the $BaTi_{1-x}Hf_xO_3$ nanopowders prepared by the modified Pechini method and annealed at 900°C for 2 hours: (a) x = 0; (b) x = 0.05; (c) x = 0.10 and (d) x = 0.20; the insets in the top-right corners of Fig. 2 (a)-(d) display the histograms indicating the particle size distributions for the investigated powders [25].

Fine-grained $BaTi_{1-x}Hf_xO_3$ ceramics consolidated by Spark Plasma Sintering

Phase purity and crystal structure of BTH ceramics

The XRD patterns in Fig. 3(a) for all the resulted ceramics reveal a perovskite single-phase structure, just like in the case of the initial BTH powders. The first detail of Fig. 3(b) corresponding to the region delimited by the light blue rectangle of Fig. 3(a) suggests a gradual change of the unit cell symmetry with the increase of Hf^{4+} addition. Thus, for the undoped BT sample, the presence of the asymmetric feature visible as a shoulder in the left side of the (200) reflection is assigned to the (002) crystalline plane, indicating a typical ferroelectric T structure (space group *P4mm*). For the BTH specimen with the lowest solute content (x = 0.05) the asymmetric profile of the (200) reflection is preserved, but with a modification of the intensity ratio of the two adjacent (002)/ (200) peaks. Unlike the undoped sample, where the intensity of (200) reflection prevails over the low-intensity (002) reflection, in the BTH05 specimen an opposite ratio is noticed. This feature is specific to the O structure (space group *Amm2*), where the first peak marked by an asterisk-type symbol in Fig. 3(b) is assigned to the (022) crystalline plane. This ratio is ~1.18 for the BTH05 ceramic, which suggests that in this composition, a mixture of T+O phases, with a slight predominance of the O modification, should be considered. This finding is supported by analyzing the second detail of Fig. 3(c), which corresponds to the region of 2θ = 73 – 76.5°, delimited by the pink rectangle in Fig. 3(a). The structural modification, as the Hf content increases from x = 0 to x = 0.05 is emphasized by the splitting of the (301)/(310) peak, specific to the T BaTiO3 in two adjacent peaks, i.e. (042)/(113) and (331), which correspond to the O distortion. These peaks, together with the (024) reflection of the O structure, which corresponds to the (103) reflection in the T polymorph, are slightly shifted to lower diffraction angles. Therefore, one can conclude that at room temperature, BTH05 composition should be placed in the proximity of the O-T phase transition.

A further increase of Hf content causes a new structural change, so that for the BTH10 and BTH20 ceramics a single peak was only detected, as shown in both detail images of Fig. 3(b) and Fig. 3(c). This suggests the presence of a single-phase ceramic with either a C or a T structure, or a double-phase composition consisting of a mixture of the two (R+C) phases. The R modification prevails in BTH10 and BTH20 specimens, but its proportion reduces; consequently, the proportion of the C phase increases, as the solute content increases. The structural analysis indicates that BTH20 sample is in the proximity of the ferroelectric-paraelectric phase transition at room temperature.

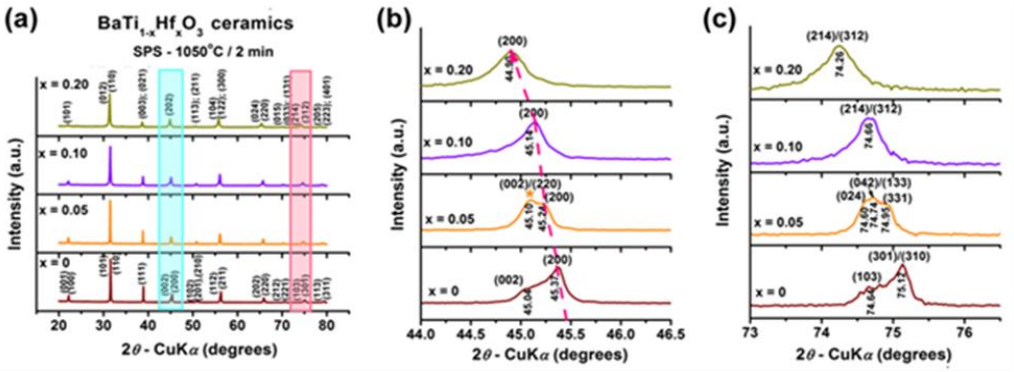


Fig. 3. (a) Room-temperature X-ray diffraction patterns of $BaTi_{1-x}Hf_xO_3$ ceramics consolidated by SPS at 1050°C for 2 min; (b) detail (the light blue rectangle of Fig. 3(a)) of the region corresponding to the diffraction angles 2θ = 44.5 - 46.5° and (c) detail (the pink rectangle of Fig. 3(a)) of the region corresponding to the diffraction angles 2θ = 73 - 76.5° [25].

The influence of Hf content on the structural parameters, specifically rising both the unit cell volume and the internal micro-strains while reducing the average crystallite size as the solute content increases, is similar to that acting in the starting BTH powders.

Microstructure

The FE-SEM image of the BT fresh fractured ceramic shows a dense, homogeneous, fine-grained microstructure, consisting of well-faceted polyhedral grains, uniform as shape and size (Fig. 4), which by strongly-welding generated almost perfect triple junctions. The pore-free sample exhibits a relative density of 99.4% and uni-modal grain size distribution, with an average grain size, <*GS*> of 0.97 μm (inset of Fig. 4(a)).

Incorporation of 5 mol.% Hf on Ti sites in BTH05 specimen induces specific disruption in the microstructure, resulting from the early fragmentation of the ceramic grains (Fig. 4(b)). This process affects the overall microstructural uniformity and causes the appearance of a small fraction of intergranular porosity, which causes the slight decrease of the relative density to 97.7%. The average grain size decreases to 0.76 μm and the grain size distribution becomes broader than one corresponding to the undoped BT sample, showing an incipient tendency toward a bi-modal type, with a major fraction (~58%) of smaller grains, with sizes below 0.6 μm, and about ~12% larger grains, with sizes ranged between (1.5 – 1.8) μm (inset of Fig. 4(b)).

The increase of the hafnium content in BTH10 and BTH20 ceramics has a remarkable effect on the grain size, which strongly decreases toward the nanometre range (Fig. 4(c) and Fig. 4(d)). Thus, <*GS*> values of 69 and 57 nm, were estimated for BTH10 and BTH20, respectively. The drop in the grain size is much steeper than one of the particle size in the starting BTH powders.

Despite their small size, the polyhedral shape and the faceting of the ceramic grains is maintained, as reveal by the insets shown in Fig. 4(c) and 4(d). Microstructural uniformity and densification are restored, while the uni-modal grain size distributions become narrower, as indicate the histograms of the insets of the mentioned figures.

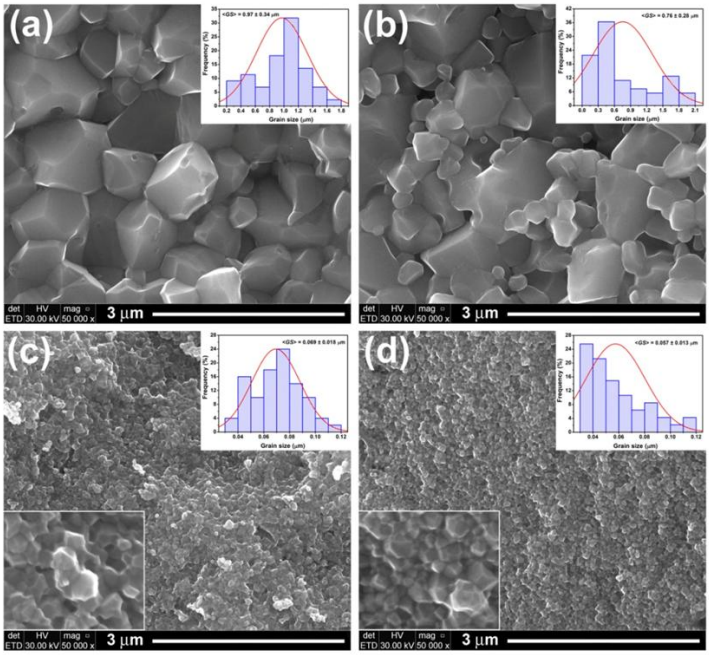


Fig. 4. (a)-(d) FE-SEM images in fracture of the $BaTi_{1-x}Hf_xO_3$ ceramics derived from the Pechini nanopowders and consolidated by SPS at 1050°C / 2 min: (a) x = 0; (b) x = 0.05; (c) x = 0.10 and (d) x = 0.20; the insets in the top-right corners of Figs. 4(a)-(d) display the histograms indicating the grain size distributions for all the ceramics under investigation; the insets in the bottom-left corners of Figs.

4(c) and 4(d) show details of the microstructure of the nanocrystalline $BaTi_{0.90}Hf_{0.10}O_3$ and $BaTi_{0.80}Hf_{0.20}O_3$ ceramics, respectively [25].

Curie-Weiss analysis

Increasing Hf content along with grain size reduction leads to a higher degree of diffuseness of the ferroelectric-paraelectric phase transition. The nature of the dispersion and the degree of the diffuseness was analyzed by using the modified Curie-Weiss equation [33]:

$$\frac{\varepsilon'_A}{\varepsilon} = 1 + \frac{(T - T_A)^\gamma}{2\delta^2} \quad (1)$$

in which ε'_A is the maximum permittivity at the corresponding temperature T_A, δ describes the temperature range over which the phase transition occurs, and γ is the diffuseness degree of the phase transition ($1 \leq \gamma \leq 2$, $\gamma = 1$ for typical ferroelectrics and $\gamma = 2$ for "full relaxor state"). The parameters ε'_A and T_A are determined by fitting the dielectric data with the Lorentzian equation (1) and are compared with the maximum permittivity ε'_m at its corresponding T_C. While ε'_A may differ slightly from the measured ε'_m, T_A is found to be close to T_C. The significant reduction in both ε'_A and ε'_m reflect the suppression of long-range ferroelectric order due to Hf doping, while the drop of T_A and T_C indicates the destabilization of the ferroelectric state caused by Hf-induced lattice distortions.

The introduction of Hf solute on Ti sites into the BT lattice generates local distortions that disrupt the long-range ferroelectric order, leading to localized polarization effects and a broader temperature range for the phase transition. The increasing broadening of the ferroelectric-paraelectric phase transition observed at higher Hf content ($0.10 \leq x \leq 0.20$) are primarily attributed to the more significant structural disorder and hence to the dilution of dipolar polarization caused by the substitution of Ti^{4+} with Hf^{4+} in the [TiO_6] octahedral framework. At higher Hf concentrations, the distortions become more pronounced, creating short-range polar regions, that weakly interact each other. This behaviour is responsible for the diffuse phase transitions and lower permittivity values observed experimentally. Furthermore, the significant lattice distortions enhance localized charge-trapping mechanisms, resulting in additional polarization relaxation processes. The attenuation of ferroelectric transitions reflects a substantial disruption of ferroelectric order, consistent with increased structural disorder and a weakening of long-range dipolar interactions. The nanostructure seems to play a key-role in diluting the ferroelectric character due to the high density of grain boundary regions, where the significant rise of the related micro-strains could induce a structural heterogeneity of the ceramic grains.

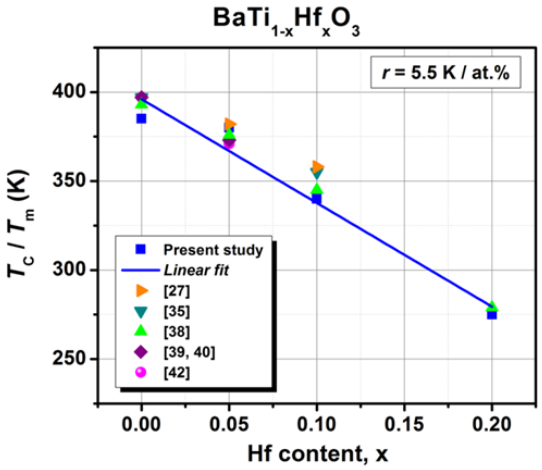


Fig. 5. Dependence of ferroelectric-paraelectric phase transition temperature, T_C / T_m, *vs.* Hf content for BTH ceramics consolidated by spark plasma sintering investigated in this study, as well as for BTH ceramics consolidated by conventional sintering, reported in the literature [25, 34-42].

It is worth to mention that the values of the ferroelectric-paraelectric transition temperature T_C / T_m for our BTH samples are slightly lower as a result of the smaller grain sizes than those reported by most of the recent papers, who investigated coarser ceramics with similar compositions, but prepared by the classical solid-state reaction method (Fig. 5.) [34-36, 40,41,43].

Ferroelectric hysteretic P(E) response

Ferroelectric $P(E)$ loops of the coarse $BaTi_{1-x}Hf_xO_3$ ceramics with a few similar compositions have been reported in refs. [34-36,41,44,45]. However, well saturated loops recorded for a high applied fields with amplitude around 30 – 45 kV/cm, to allow a comparison of their characteristics, are presented only in refs. [34-36]. All the investigated ceramics sustained the application of a high field of ~50 kV/cm amplitude, enough to provide saturation and to exhibit a stable polarization-field switching response, with symmetrically shaped and well-closed hysteresis loops. With respect to the $P(E)$ loops reported in literature for coarse BTH ceramics, all the BTH ceramics under investigation show lower values for the hysteresis loop area, rectangularity factor P_r/P_S (below 0.16) and similar values as in literature for the coercive field (E_C) (Fig. 6 (a), (b)) [34-36]. The remanent polarization P_r takes values below 5 μC/cm^2 for all the fine-grained investigated BTH compositions (Fig. 6(b)), while for coarse ceramics with similar or close compositions, larger values have been reported in literature: 12 – 15 μC/cm^2 (for Hf: 5% and 11%) [35], 14 μC/cm^2 (5% Hf) and 8 μC/cm^2 (12% Hf) [36], 7 – 10 μC/cm^2 (2% Hf) [45].This result represents a typical grain size effect, as ones recorded in BT-based ceramics when reducing their grain size at nanoscale [32,46-49].

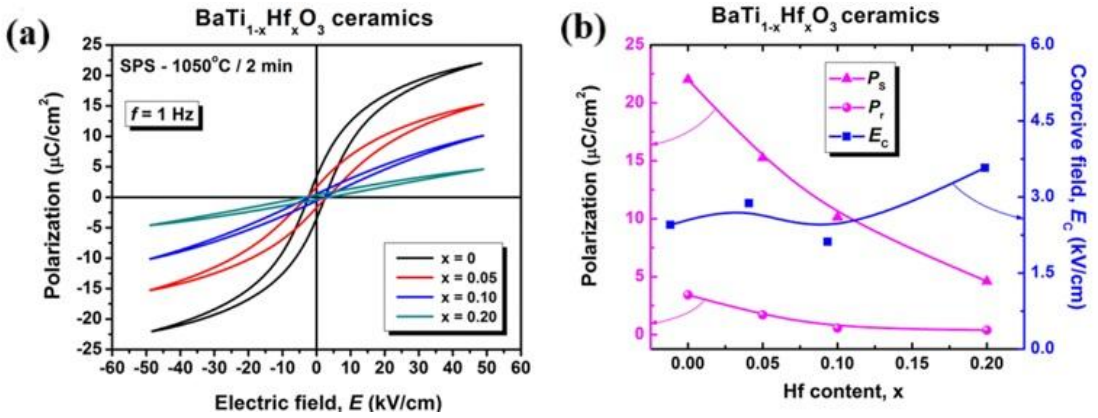


Fig. 6. (a) comparative hysteresis loops for $BaTi_{1-x}Hf_xO_3$ (x = 0; 0.05; 0.10; 0.20) ceramics recorded at the maximum applied electric field and (b) P_S, P_r, and E_C evolution *vs*. Hf content corresponding to BTH ceramics [25].

The $P(E)$ hysteresis loops become progressively less saturated and more tilted when increasing the Hf addition, so that the rectangularity factor decreases down to 0.08 value for BTH20. The polarization response is scaled down with Hf addition, with a saturation polarization from P_S ~ 22 μC/cm^2 in pure BT ceramic to P_S ~ 10 μC/cm^2 for the composition x = 0.10. The composition BTH20 shows a very tiny hysteretic behaviour, but still presents a very small non-linearity. This tendency demonstrates the gradual transformation of the dipolar entities from long-range-order ferroelectric character to the relaxor state characterized by nanoscale polarization, which is characterized by practically zero coercivity. The small polarization values and the slim and tilted hysteresis loops are also a consequence of the approaching at room temperature the range for the ferroelectric-to-paraelectric transformation when increasing the Hf addition, and is also a characteristic of the nanostructured BT-based ceramics [32,46-50].

Short-range ordering and evolution of phase transitions vs. temperature by Raman spectroscopy investigations

Raman spectroscopy is a powerful tool, very sensitive in detecting local distortions in perovskite systems where disorder or disruption in crystalline lattice occurs due to doping or to nanoscale structuring.

To follow the evolution of the structure and to monitor phase transitions in BTH ceramics, the temperature dependence of Raman scattering was recorded in the temperature range of (148 - 473) K. The diagram of Fig. 7 shows the temperature dependence of the "silent" mode frequency for BT and BTH05. The presence of three domains of phase-overlapping, *i.e.* (R+O), (O+T) and (T+C), were noticed. Compared to BT, for BTH05 sample the (R+O) and (O+T) domains are shifted to higher temperature values and become broader, while the (T+C) domain become narrower and shifted to lower temperature. This is consistent with the opposite variation of both the low-temperature phase transition temperatures T_1 and T_2, relative to the ferroelectric-paraelectric phase transition temperature, T_C, in homovalently *B*-site substituted $BaTiO_3$ ceramics. In the diagram of Fig. 7 the temperature values of the three phase transitions determined from temperature dependence of the dielectric constant are marked by dashed lines inside the di-phase domains. Domains of coexistence of crystalline phases with dissimilar symmetries were also reported in homovalently *A*-site doped barium titanate, as some $(Ba,Sr)TiO_3$ solid solutions [26,51].

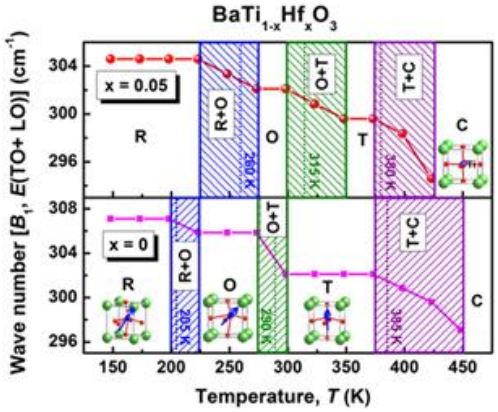


Fig. 7. Temperature dependence of frequency of [B_1, E(TO+LO)] mode in BT and BTH05 ceramics [25].

The increase of Hf content in BTH10 determines obvious structural changes. Thus, at 248 K the R phase was detected by the corresponding low-temperature features.

Increasing solute proportion up to x=0.20 induces the shift of [A_1(TO)], [A_1(TO), E(TO)] and [A_1(LO), E(LO)] modes to higher frequencies. The presence of the "silent" mode is not detectable even at lower temperatures, but instead, [A_1(TO)] band exhibits a right-side asymmetric profile and a significant shift to ~289 cm^{-1}.

The difference in the evolution of Raman scattering of BTH10 and BTH20 could be explained in terms of the specific features related to the "pinched" ferroelectric-paraelectric phase transition in the two mentioned compositions. The increased Hf content in BTH20 compared to BTH10 therefore causes not only the equivalent T_m fall from 345 to 325 K, but also a more pronounced diffuseness of the phase transition, as indicated by the permittivity data *vs*. temperature. BTH10 evolves more steeply towards the paraelectric phase than BTH20, which seems to maintain a less pronounced but more stable polar order far above T_m. This finding supports the assumption that randomly distributed nano-sized polar clusters embedded in a cubic matrix as in a relaxor-like state, may occur at high temperature, prior to

the development of a typical paraelectric state, which seems not to have been reached yet at the maximum temperature used for the Raman scattering investigations carried out in this study.

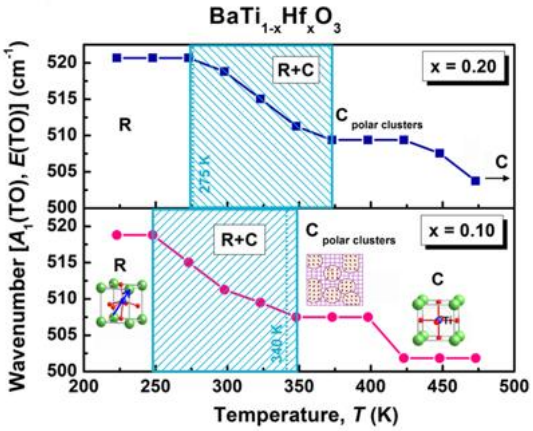


Fig. 8. Temperature dependence of frequency of [A_1(TO), E(TO)] mode in BTH10 and BTH20 ceramics [25].

The diagram of Fig. 8 based on thermo-Raman scattering data, which presents the temperature dependence of frequency for the [A_1(TO), E(TO)] mode in BTH10 and BTH20 samples reveals in both cases a wide temperature domain in which R and C polymorphs coexist. This domain, as well as the one corresponding to the polar nanoregions, is shifted towards higher temperatures in BTH20, compared to the BTH10 sample.

The presence of di-phase domains in the fine-grained SP-sintered BTH ceramics examined in this work allowed proposing a low-temperature phase diagram of the $BaTiO_3$–$BaHfO_3$ system, based on both the thermo-Raman scattering and dielectric data (Fig. 9).

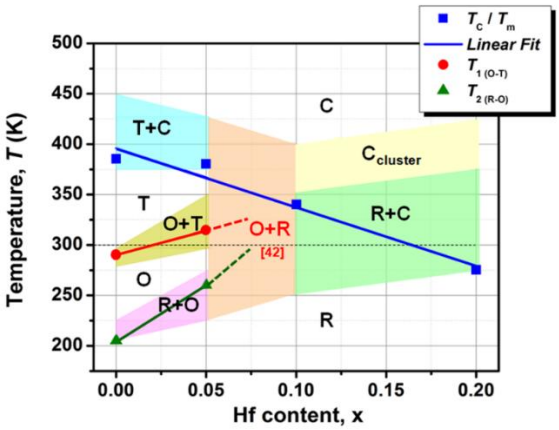


Fig. 9. Proposed phase diagram for the $BaTiO_3$ – $BaHfO_3$ system, based on both the data of low-field dielectric analysis and Raman spectroscopy results, for SP-sintered BTH ceramics derived from nanopowders synthesized by the modified Pechini method [25].

2. Influence of grain size on the functional properties in multiscale-structured Pechini $BaTi_{0.90}Hf_{0.10}O_3$ (BTH10) ceramics

Composition dependent on structural feature and properties in BTH10 ceramics

The staring BTH nanopowder, the ceramic samples resulted after consolidation by alternative strategies are free of residual Ba- or Ti-rich phases, consisting only of well-crystallized perovskite $BaTi_{0.90}Hf_{0.10}O_3$ solid solution, as shown in Fig.10(a), (d) and (g).

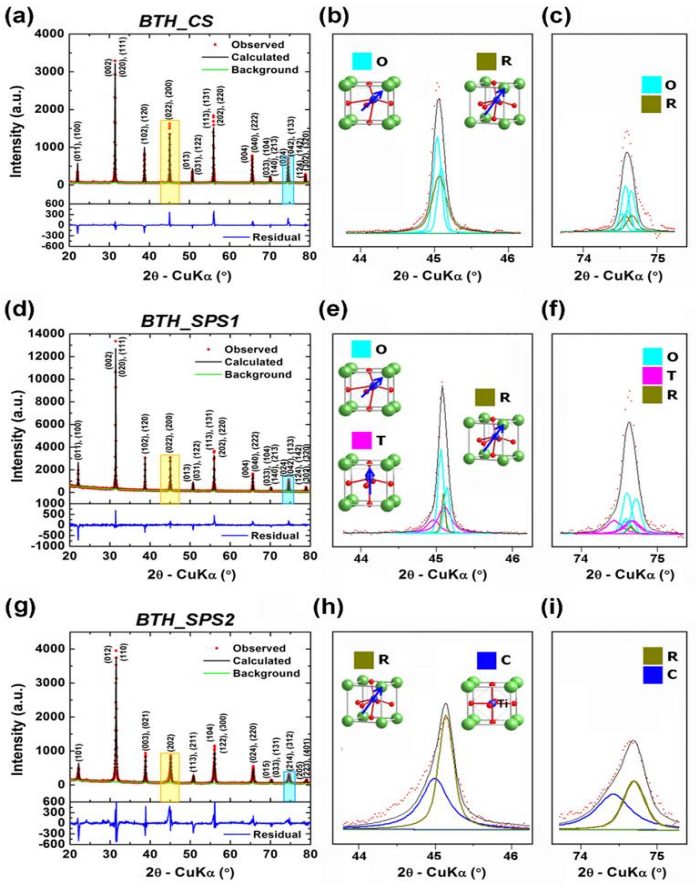


Fig. 10. (a)-(c) Room-temperature X-ray diffraction patterns for $BaTi_{0.90}Hf_{0.10}O_3$ ceramics consolidated by different strategies: (a) conventional sintering at 1400°C / 4 h (*BTH_CS*), (d) spark plasma sintering at 1200°C / 2 min (*BTH_SPS1*), (g) spark plasma sintering at 1050°C / 2 min (*BTH_SPS2*); (b), (e), (h) details (the yellowish rectangles of Fig.10 (a), (d), (g)) of the region corresponding to the diffraction angles 2θ = 43.7 - 46.2° and (c), (f), (i) details (the light blue rectangles Fig.10 (a), (d), (g)) of the region corresponding to the diffraction angles 2θ = 73.7 - 75.5°, showing the coexistence of BTH phases with different symmetries [52].

At room temperature, a mixture of a major (O) phase and a significantly lower amount of (R) phase was found for the ceramic sample (*BTH_CS*) obtained by conventional sintering, as indicates the deconvolution of the reflections located at ~45° and ~75° in the corresponding pattern (Fig.10 (b), (c)), which also corresponds to the phase superposition determined for the stress-free coarse $BaTi_{0.90}Hf_{0.10}O_3$ ceramic by Landau free-energy calculations. For the BTH specimens consolidated by spark plasma sintering (SPS), the crystalline structure depends on the sintering temperature. Thus, a three-phase composition, consisting of a mixture of close proportions of orthorhombic (O) and tetragonal (T) modifications (O: 48.4%, T: 43.2%), together with a small amount of rhombohedral (R: 8.4%) polymorphs, was detected for the (*BTH_SPS1*) sample sintered at higher temperature (Fig. 10(e), (f)), while in the specimen SP-sintered at 1050°C (*BTH_SPS2*), a two-phased composition with R and C polymorphs was found (Fig. 10(h), (i)).

The microstructure strongly depends on the sintering strategy used to consolidate the ceramic bodies, as reveal the FE-SEM images of Fig. 11. All the specimens exhibit dense and homogeneous microstructures, with equiaxed grains, uniform as shape and size (Fig.11(a), (b), (c)).

The histograms depicted as insets in the bottom-right corners of Fig.11(a), (b), (c) indicate unimodal grain size distributions. <*GS*> values of 3.7 μm, 2.8 μm and 0.07 μm were estimated for the samples *BTH_SPS1*, *BTH_CS* and *BTH_SPS2*, respectively. Thereby, it was found that, no matter of the

consolidation technique, coarse-grained samples, with the average grain size in the micron range, resulted after sintering at higher temperatures of 1400°C / 4 h for CS and 1200°C / 2 min for SPS (Fig. 11(a), (b)), whereas a fine-grained specimen, with <*GS*> downscaled in the nanometre range, was obtained after SPS at 1050°C / 2 min (Fig. 11(c)).

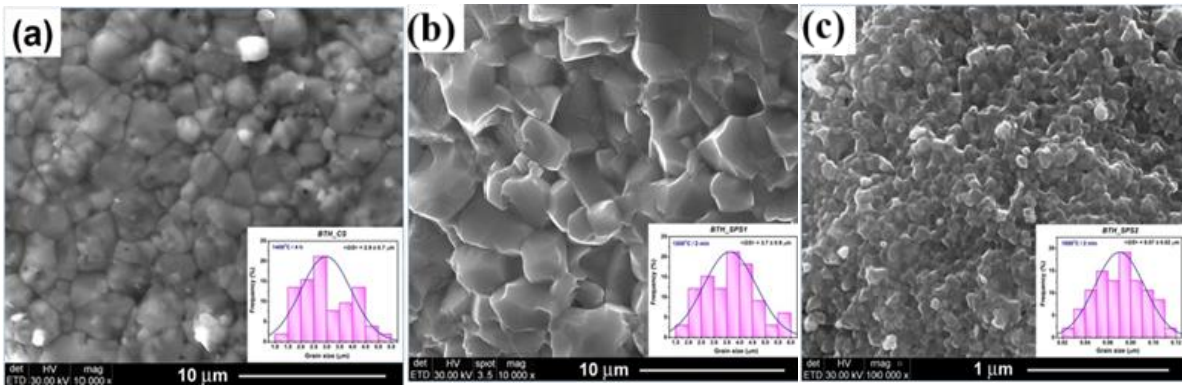


Fig. 11. FE-SEM images of different magnifications: (a), (b), (c) images of lower magnifications: (a), conventional sintering at 1400°C / 4 hours (sample *BTH_CS*); (b) spark plasma sintering at 1200°C / 2 min (sample *BTH_SPS1*) and (c) spark plasma sintering at 1050°C / 2 min (sample *BTH_SPS2*); the insets in the bottom-right corners of Fig. 11(a), (b) and (c) display the histograms indicating the grain size distributions [52].

The observed phase composition and microstructural differences are related to the differences between the involved sintering methods. With respect to the conventional sintering, which takes place by a slow equilibrium densification process allowing the grain growth and equilibration of defects and of the local strain-stress fields, SPS provides a fast, non-equilibrium consolidation mechanism. Their relative densities are higher: 99.7% (BTH_SPS1) and 98.8% (BTH_SPS2), with respect to 94% for the ceramic (BTH_CS), which cause a higher level of the internal stress, also. The significant proportion of C modification found in the nanocrystalline BTH_SPS2 ceramic could be explained in terms of a faster evolution toward the ferroelectric-paraelectric phase transition as a result of GS reduction [46], together with the high strains exerted in the grain boundary regions induced by nanostructuring.

The influence of the size effect in BTH10

$BaTi_{0.90}Hf_{0.10}O_3$ ceramics consolidated by the three sintering strategies already mentioned were analyzed from the point of the influence of grain size on the low- and high-field dielectric properties. The low-field measurements allow to trace the evolution of the dielectric response across the ferroelectric-paraelectric transition and to identify features associated with domain dynamics, phase transitions, and relaxation mechanisms, highlighting the role of grain size, morphology and densification in shaping the dielectric response.

The temperature-dependent dielectric response was analyzed over a broad frequency range (10^2 Hz - 10^6 Hz) for the BTH ceramics with various grain sizes in terms of the real part of the permittivity (ε') (Fig.12(a), (b)).

The coexistence of various structural modifications in a more or less broadened temperature range as a result of the proximity and diffuseness of the ferroelectric-to-paraelectric phase transition has also been reported for 10 at.% Hf^{4+}-doped BTH ceramics obtained by the classical solid state reaction method [53-55]. Thus, the prominent peak observed around 345 K in the temperature dependence of the real part of the dielectric permittivity (ε') in Fig.12(a) corresponds to the ferroelectric-paraelectric phase transition of the $BaTi_{0.90}Hf_{0.10}O_3$ ceramic sample sintered *via* spark plasma sintering at 1200°C/2 min (*BTH_SPS1*). The sharpness of the transition, as well as the high maximum permittivity values (~6510 at 100 Hz) indicates that the material retains a well-defined long-range ferroelectric order. The

position of the permittivity maximum is not frequency-dependent and remains constant across the investigated frequencies. Anyway, the inset of Fig. 12(a) provides a zoomed-in view of the transition region and highlights a subtle frequency dispersion of $\varepsilon'(T)$ in the temperature range just below the transition. Thus, while the Curie temperature (T_C) is unchanged, the permittivity values below T_C show increasing separation with decreasing frequency.

Compared to the almost perfectly densified *BTH_SPS1* sample, the conventionally sintered $BaTi_{0.90}Hf_{0.10}O_3$ specimen (*BTH_CS*) exhibits a ferroelectric-paraelectric phase transition with a significantly lower permittivity maximum (~3352 at 10^2 Hz), located at $T_C \approx 340$ K (Fig. 12(b)). Although the grain size in both samples is comparable, the conventionally sintered ceramic displays a lower overall densification reflected in a higher amount of porosity of ~ 6%. Consequently, the reduction in permittivity is attributed to the increased porosity and reduced effective polarizability, specific to the conventionally sintered ceramics.

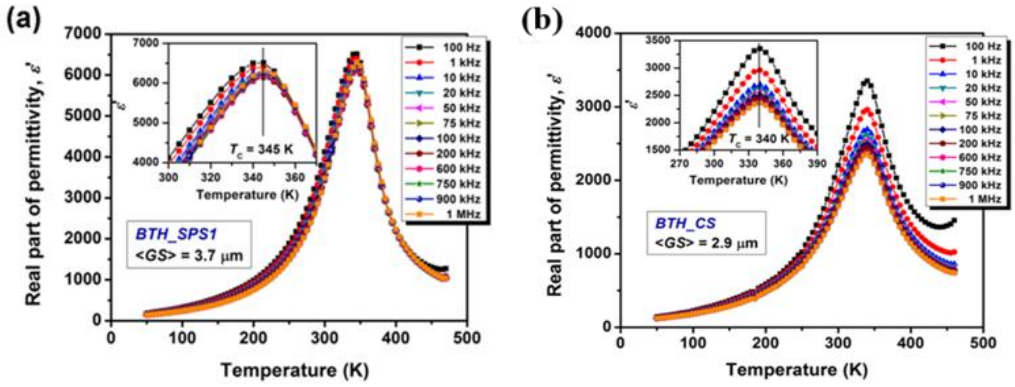


Fig. 12. Temperature dependence of the dielectric response: (a), (b) the real part of permittivity (ε') for BTH ceramics with various grain sizes (<*GS*>): (a) *BTH_SPS1*, <*GS*> = 3.7 μm; (b) *BTH_CS*, <*GS*> = 2.9 μm [52].

The phase transition appears broader and more diffuse, with $\varepsilon'(T)$ curves exhibiting frequency dispersion on both sides of T_C. The permittivity decreases with increasing frequency, from ~3352 at 10^2 Hz down to ~2357 at 10^6 Hz, yet the temperature of the dielectric maximum remains unchanged, indicating that the material does not exhibit relaxor behaviour.

(P-E) hysteresis loops and energy storage performance

It is clear that the different sintering strategies which provided samples with dissimilar structural modifications and microstructures play an important role on the hysteretic response. The ceramic *BTH_CS* sample consolidated by conventional sintering presents a large hysteresis loop with smaller polarization $P_r = 5.5$ μC/cm^2, $E_C = 10$ kV/cm and $P_r/P_S = 0.49$, whose switching behaviour is related to the O and R phase superposition, to the 6% porosity level and also contain a high-field resistive lossy contribution.

The hysteretic response of the dense, nanostructured *BTH_SPS2* ceramic is characterized by a very slim and tilted loop, with small hysteresis area and low non-linearity, with respect to that one of *BTH_SPS1*. The *P*(*E*) loop is still not completely saturated at 50 kV/cm field amplitude, for which the remanent polarization is $P_r = 0.55$ μC/cm^2, the coercive field of $E_C = 2$ kV/cm and rectangularity factor $P_r/P_S = 0.05$.

The loop tilting towards a non-hysteretic polarization-field response determined for the *BTH_SPS2* ceramics can be comprehended by the three combined factors induced by the Hf addition and SPS sintering consolidation: the approaching of ferroelectric-relaxor crossover, the *GS* reduction down to nanoscale and the approaching of the paraelectric state around room temperature, as indicated by the presence of C polymorph.

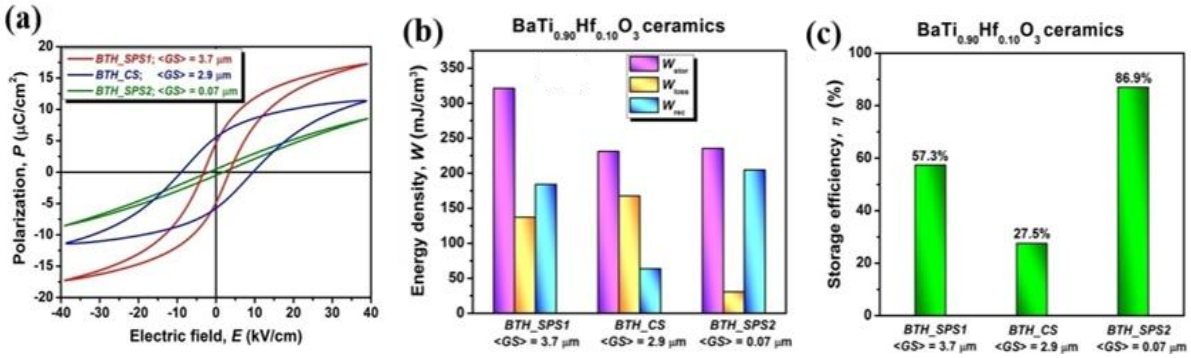


Fig. 13. (a) comparative hysteresis loops for the $BaTi_{0.90}Hf_{0.10}O_3$ ceramics produced by various consolidation methods recorded at the maximum applied electric field; energy storage characteristics: (b) energy storage density (W_{stor}), energy loss density (W_{loss}) and recoverable energy density (W_{rec}) and (c) storage efficiency (η), estimated for the applied field E = 50 kV/cm [52].

The influence of grain size, *GS* on these properties is revealed in Fig.13(b)-(c). Among the BTH investigated samples, it is noticed the advantage of using SPS consolidation in providing higher energy densities and lower energy loss, thus inducing high storage efficiency with respect to the classical sintering sample. The ultrafine nanocrystalline *BTH_SPS2* ceramic has a storage efficiency η of 86.9%, which is superior to the one reported for fine-grained $Ba_{0.6}Sr_{0.4}TiO_3$ ceramics with almost similar grain size, investigated in the past (η ~70%) [51]. Both the SP-sintered BTH ceramics have storage performances similar to those ones reported for other $BaTiO_3$-based ceramics [19].

3. Influence of the grain size on the functional properties in fine-grained $Ba_{0.80}Sr_{0.20}TiO_3$ (BST20) and $Ba_{0.60}Sr_{0.40}TiO_3$ (BST40) ceramics

As in the case of $Ba(Ti,Hf)O_3$ (BTH) ceramics, investigating the influence of grain size on the functional properties of fine-grained (Ba,Sr)TiO3 (BST) ceramics requires preparation by wet-chemical routes of pure and homogeneous starting BST nanopowders. For this study, two BST compositions described by the nominal formulae $Ba_{0.80}Sr_{0.20}TiO_3$ (BST20) found at room temperature in the ferroelectric state and $Ba_{0.60}Sr_{0.40}TiO_3$ (BST40) found at RT in the paraelectric state, were chosen.

Microstructure of $Ba_{0.80}Sr_{0.20}TiO_3$ (BST20) and $Ba_{0.60}Sr_{0.40}TiO_3$ (BST40) ceramics

To analyze the microstructural features, FE-SEM investigations were performed for all the fine-grained BST20 and BST40 ceramics, while to highlight possible structural and compositional gradients, TEM, HRTEM, SAED and EDX investigations were carried out on the 2BST sample with a grain size of 179 nm.

The FE-SEM images of all the fine-grained BST20 ceramics obtained by SPS (Fig.14(a)-(c)) show dense microstructures, consisting of equiaxed grains, more uniform in shape and size and presenting a narrower unimodal size distributions (insets of Fig.14(a)-(c)) [26]. The increase in grain size obtained by increasing the SPS temperature/plateau determines a better densification by decreasing the intergranular porosity. Besides, it contributes to a change in grains' shape, which evolves from a more rounded morphology to a better faceted one, with well-defined edges and corners, so that the 3BST sample, with a grain size of 234 nm, exhibits almost cuboidal grains.

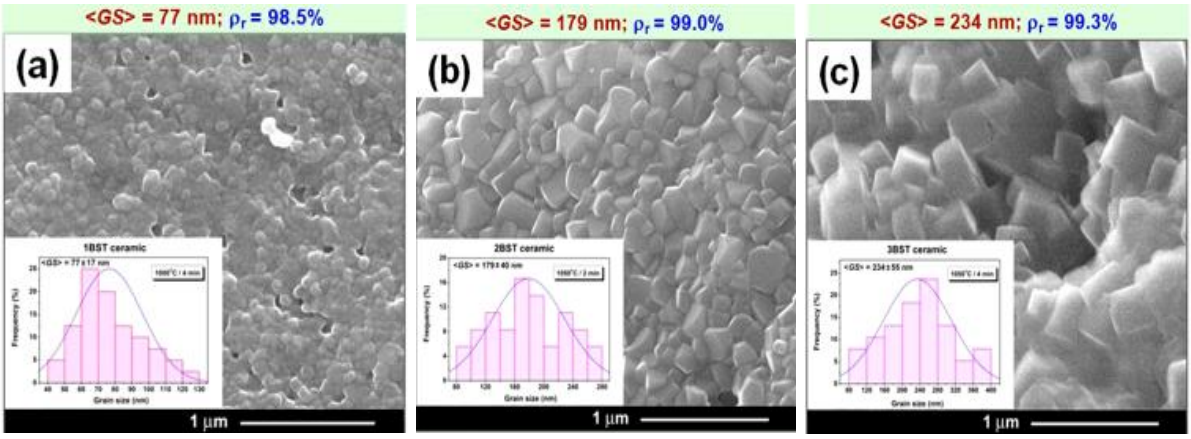


Fig. 14. FE-SEM images in fracture of the sol-gel of BST20 ceramics with various grain sizes: (a) **1BST**: <*GS*> = 77 nm [26]; (b) **2BST**: <*GS*> = 179 nm [26]; (c) **3BST**: <*GS*> = 234 [26] nm

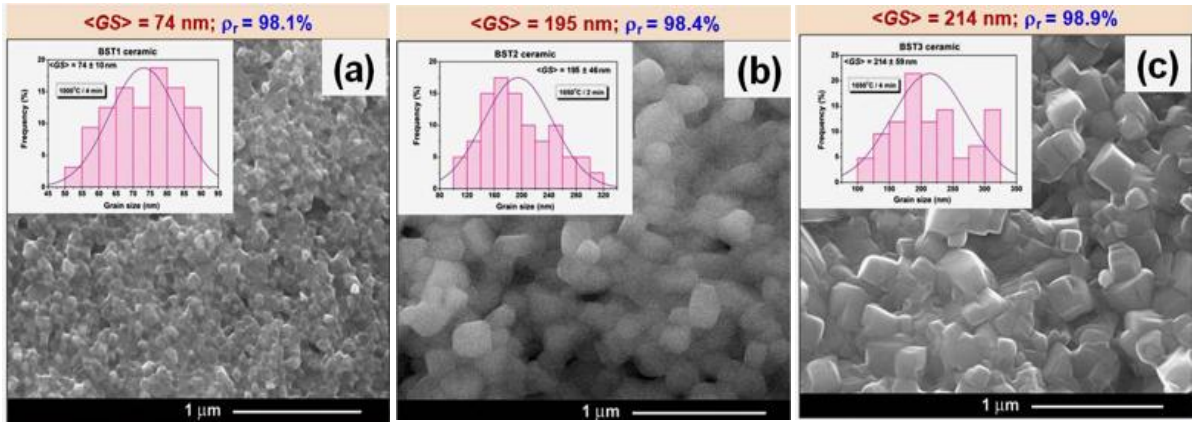


Fig. 15. FE-SEM images in the fracture of the sol-gel BST40 ceramics with various grain sizes: (a) **BST1**: <*GS*> = 74 nm [51]; (b) **BST2:** <*GS*> = 195 nm [51]; (c) **BST3:** <*GS*> = 214 nm [51]

FE-SEM investigations of the fine-grained BST40 specimens show that, the ceramic sample obtained by SPS at 1000°C for 2 min (BST1) exhibits an average grain size <*GS*> of 74 nm, very close to the average particle size $<d_{SEM}>$ ~ 73 nm found in the starting BST40 nanopowder, suggesting that during the SPS process grain growth is strongly inhibited by the high heating rate (Fig. 15(a)). The increase of both the SPS temperature from 1000 to 1050°C and the SPS plateau from 2 to 4 min results in the increase of grain size in the submicron range. Thus, <*GS*> values of 195 and 214 nm were estimated for the ceramics consolidated by SPS at 1050°C/2min (BST2) and 1050°C/4 min (BST3), respectively (Fig. 15(b) and Fig. 15(c)) [51]. This increase in grain size is accompanied by a slightly higher densification, due to the removal of the intergranular porosity. Anyway, high relative density values ranging between 98 and 99% were determined for all the fine-grained BST40 ceramics. As in the case of the fine-grained BST20 ceramics, with increasing grain size, a trend towards a cuboidal grain morphology was observed (Fig. 15(a)-(c)). Unimodal grain size distributions (insets in Fig. 15(a)-(c)) were also obtained for the fine-grained BST40 specimens.

To prove the "brick-wall"-type structure of such small grains in the ferroelectric 2BST ceramic, further TEM/HRTEM investigations coupled with SAED analyses were performed (Fig.16(a)-(g)).

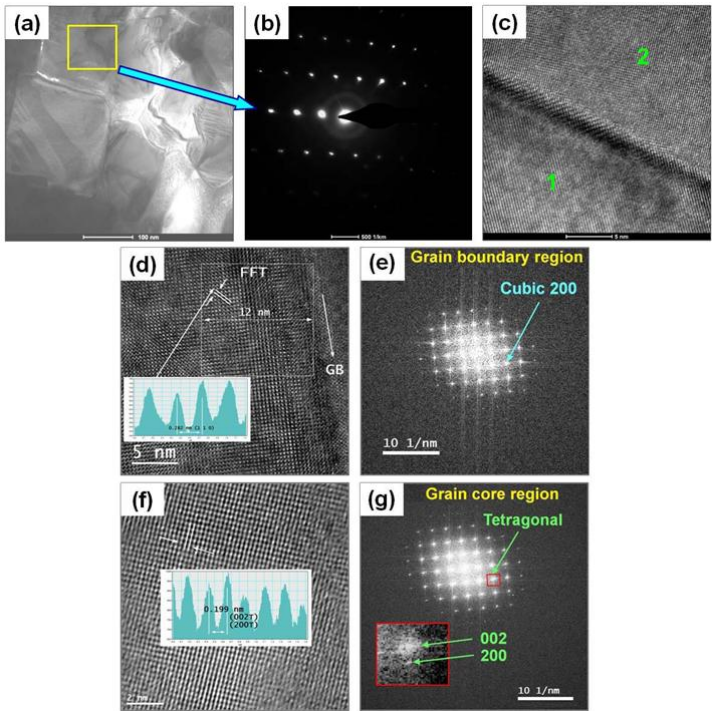


Fig. 16. (a) TEM image; (b) SAED pattern, showing the single-crystal nature of the grain marked by yellow rectangle in Fig. 16(a); (c) HRTEM image showing details of the grain- boundary region between two adjacent grains denoted as 1 and 2; (d), (f) HRTEM images and (e), (g) related Fast Fourier Transform (FFT) patterns for: (d), (e) an area inside a layer of 12 nm thickness, adjacent to the grain boundary GB, marked by the white-lined square and (f), (g) grain core region: inserts of Fig. 16(d), (f) – measurements of *d*-spacing and inset of Fig. 16(g) – enlarged view of the area marked by the red-lined square inside the FFT pattern related to the grain core, showing the presence of the neighbouring (002) and (200) crystalline planes, specific to the tetragonal structure [26].

The TEM image of Fig. 16(a) shows the presence of some tightly-packed, polyhedral grains, also observed in the FE-SEM image of Fig. 16(b). These grains appear as single-crystals, taking into account the row-aligned bright spots, specific to the crystalline planes, in the related SAED pattern of Fig. 16(b). The higher average grain size <GS> = 179 nm compared to the average crystallite size <D> ~ 67 nm indicates that the crystals are divided into 2 – 3 crystallites, most likely because of the presence of low-angle boundary defects. The HRTEM image of Fig.16(c) displays a grain-boundary region between two adjacent grains, denoted by 1 and 2. Two different regions inside grain 1 were chosen to analyze the crystal structure: (i) the area marked by the white-lined square in Fig.16(d) located inside a 12 nm thick layer adjacent to the grain boundary and (ii) a region of the grain core (Fig.16(f)).The related Fast Fourier Transform (FFT) patterns of Fig.16(e) and Fig.16(g) reveal a cubic structure in the area adjacent to the grain boundary (Fig. 16(e)) and a tetragonal structure, pointed out by the neighbouring spots (red-lined rectangle in Fig. 16(g)) attributed to the specific (002) and (200) crystalline planes (inset of Fig. 16(g)) in the region of the grain core. Therefore, it can be stated that, based on HRTEM / FFT investigations, the "composite"-like structure of the ceramic grains was confirmed [26].

The increase of Sr content also causes an increase in the intensity of the small bands located at 571 and 620 cm^{-1}, indicating a higher lattice disorder, which originates from the higher degree of Sr substitution. Given the increasing stresses exerted in the grain boundary regions as the grain size decreases to the nanometre range, it is difficult to estimate whether the cubic structure in these "dead layers" is similar to that of the matrix in the grain cores. Considering the pinning effect exerted by the

grain boundary regions on the polarization switching, these "dead layers" can be considered non-ferroelectric, although the hypothesis of some complex distortions induced by the high stresses in these regions cannot be completely excluded. Based on the XRD, HRTEM and Raman data at RT, schematic representations of the structural characteristics of grains belonging to both ferroelectric BST20 and paraelectric BST40 ceramics were proposed (Fig. 17(a), (b)).

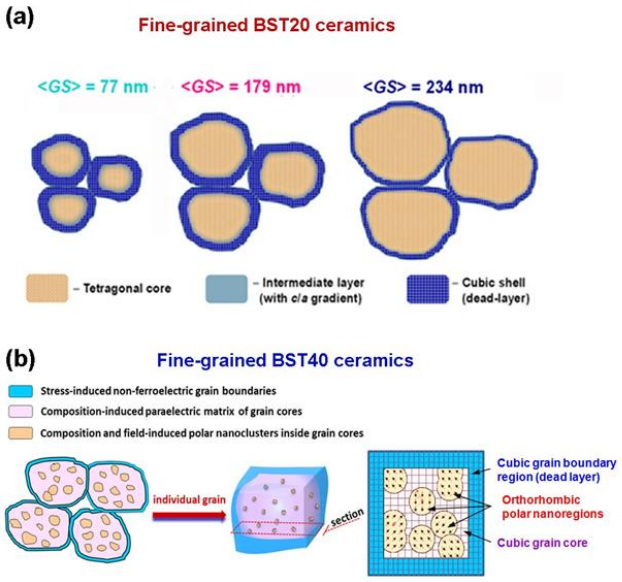


Fig. 17. Schematic representation of ceramic grains sub-structuring in: (a) fine-grained BST20 ceramics [26] and (b) fine-grained BST40 ceramics [51].

Functional properties of the sol-gel BST20 and BST40 ceramics

Thermally activated phenomena (Maxwell-Wagner interfacial polarization) determine the increase of dielectric losses at temperatures above 350 K in the low-frequency range, for all the fine-grained BST1, BST2 and BST3 ceramics. This feature, specific to ferroelectrics, is associated with the ionic conductivity and is well-known as the "low-frequency dielectric dispersion" [56]. Thermally-induced ionic conductivity is enhanced in fine-grained ceramics as a consequence of the increased volume of non-ferroelectric grain-boundary regions where surface charges agglomerate.

To have a comparative picture regarding the influence of grain size on the dielectric properties, the variation of dielectric constant (Fig.18(a), (b)) *vs.* temperature at a selected frequency of 20 kHz for the three average grain size values for each of the BST20 and BST40 ceramic samples were plotted.

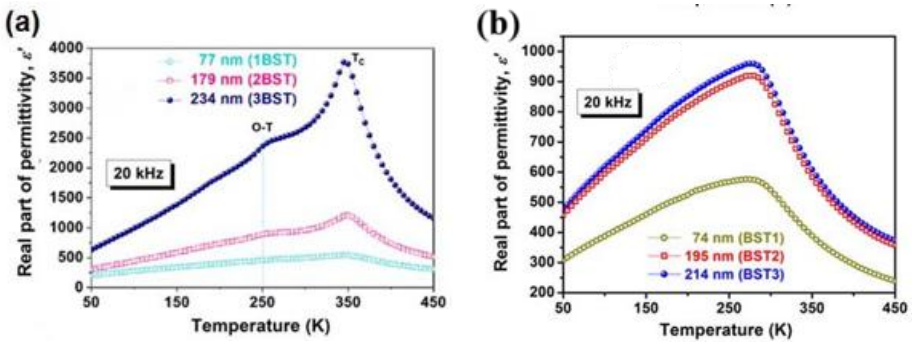


Fig. 18. Temperature dependence of dielectric properties at 20 kHz: (a), (b) real part of permittivity (ε') for: (a) BST20 ceramics and (b) BST40 ceramics with various grain sizes [26,51].

In the paraelectric state, permittivity obeys the well-known Curie-Weiss law [1,57]:

$$\varepsilon = \frac{C}{T - T_0}, \tag{2}$$

where ε is the dielectric constant, C represents the Curie constant, T is the absolute temperature, and T_0 is the Curie-Weiss temperature. The deviation from the typical Curie-Weiss law is given by the relation: $\Delta T_{\mathrm{m}} = T_{\mathrm{C-W}} - T_{\mathrm{C}}$, where $T_{\mathrm{C-W}}$ represents the temperature from which the permittivity starts to follow the Curie-Weiss law in the paraelectric state, and T_{C} is the temperature at which the phase transition takes place. The Curie-Weiss law is representative for typical coarse-grained ferroelectric ceramics, characterized by sharp ferroelectric-paraelectric phase transitions.

To estimate the degree of diffuseness of the ferroelectric-paraelectric phase transition in fine-grained and/or heavily-substituted $BaTiO_3$-based ceramics, a modified law was proposed by Uchino [58]:

$$\frac{1}{\varepsilon} - \frac{1}{\varepsilon_{\mathrm{m}}} = \frac{(T - T_{\mathrm{C}})^{\gamma}}{C} \tag{3}$$

where C is the Curie constant, T_0 is the Curie-Weiss temperature, ε_{m} is the maximum value of the dielectric constant reached at T_{C} and γ is a parameter that indicates the degree of diffuseness of the ferroelectric-paraelectric phase transition.

Fig. 19(a)-(d) presents, for the 2 categories of fine-grained ceramics BST20 and BST40, two approaches for Curie-Weiss analysis, (*i*) using the classical Curie-Weiss law and (*ii*) with the modified Curie-Weiss law.

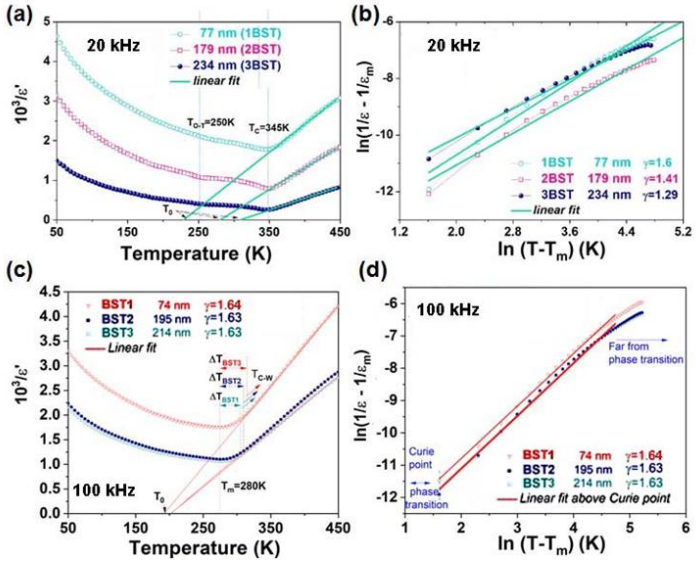


Fig. 19. Analysis performed according to the: (a), (c) usual Curie-Weiss law and (b), (d) modified Curie-Weiss law for the: (a), (b) fine-grained BST20 (at 20 kHz) and (c) (d) fine-grained BST40 ceramics (at 100 kHz) [26,51].

For both fine-grained BST20 and BST40 ceramics, increasing grain size leads to an increase in the Curie constant (C) and Curie-Weiss temperature (T_0) values and a decrease in the diffuseness degree γ of the ferroelectric-paraelectric phase transition, indicating an evolution toward a more pronounced ferroelectric state, specific to microstructured ceramics. The decrease of γ value with increasing grain size is more evident in BST20 due to the lower solute content, which favours the ferroelectric state over the relaxor state.

4. Investigation of functional properties of 5 mol% Ce^{3+}-doped $BaTiO_3$ (BCT) thin film prepared by the sol-gel method

$BaTiO_3$ is a technologically relevant material in the perovskite oxide class with above-room-temperature ferroelectricity and a very large electro-optical coefficient, making it highly suitable for emerging electronic and photonic devices. To enhance the dielectric, ferroelectric, optical, and tunability properties of thin films, it has been proposed to create multi-layered films using multiple identical deposition–annealing cycles and doping the $BaTiO_3$ lattice [59].

Doping in $BaTiO_3$-type ceramics plays an important role in the improvement of their performance [60]. The effect of Ce doping in $BaTiO_3$ ceramic materials has shown promising dielectric properties such as a relatively high permittivity, a decrease in Curie point temperature, and high endurance.

One of the objectives of the thesis was to prepare by the sol-gel method coupled with the spin-coating deposition technique a $Ba_{0.95}Ce_{0.05}Ti_{0.9875}O_3$ (BCT) thin film without cracks, with good adhesion to the substrate, well crystallized, with a smooth surface, with stoichiometric chemical composition, and with good functional properties. The configuration of the $Si/SiO_2/TiO_2/Pt/Ce^{3+}$-$BaTiO_3$ heterostructure is shown in Fig. 20. In this heterostructure, on the top of the Si(100) wafer with a thickness > 200 μm, a layer of SiO_2 was obtained by thermal corrosion in order to better control the interface. Onto the SiO_2 layer, an ultra-thin TiO_2 film was deposed as buffer layer and, finally, prior to the sol-gel BCT thin film deposition, a Pt layer with a thickness of 100 nm was sputtered to obtain the bottom electrode for the BCT thin film.

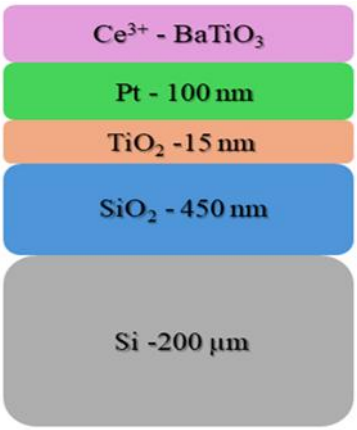


Fig. 20. Component layers of the $Si/SiO_2/TiO_2/Pt/$ BCT heterostructure [61].

Phase composition and microstructure of the BCT thin film

The XRD pattern of $Ba_{0.95}Ce_{0.05}Ti_{0.9875}O_3$ thin film deposited on Si-Pt substrate and calcined at 700°C for 1 hour, in air is presented in Fig. 21.

The XRD reflections of the $Ba_{0.95}Ce_{0.05}Ti_{0.9875}O_3$ thin film calcined at 700°C for 1 hour, in air, correspond to a single-phase perovskite structure. No secondary phases were detected. The presence of sharp peaks indicates a well-crystallized thin film.

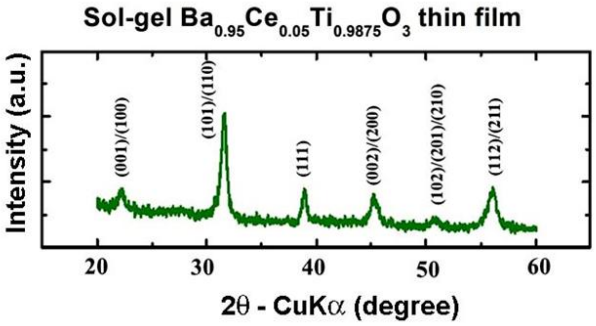


Fig. 21. X-ray diffraction pattern at room temperature for the BCT thin film calcined at 700°C, 1 h in air [61].

The slight shift in peaks positions compared to undoped $BaTiO_3$ suggests the complete solubilisation of cerium into the perovskite lattice. Ce^{3+} substitution for Ba^{2+} can induce lattice distortion, slightly shifting the diffraction peaks. According to Fig. 21, the thin film of $Ba_{0.95}Ce_{0.05}Ti_{0.9875}O_3$ shows a polycrystalline structure, without any preferential orientation for crystallization. The film is well crystallized and exhibits a pseudocubic structure, with lattice parameters $a = c = 4.0281(14)$ Å. Doping with Ce^{3+} often causes distortions of the unit cell. The volume of the unit cell is $V = 65.36$ Å^3, and the average crystallite size $\langle D \rangle = 293(36)$ Å. This is a bit smaller than the volume of the undoped $BaTiO_3$ (typically ~65.8 – 66 Å^3), indicating a slight lattice contraction, which suggests that Ce^{3+} (ionic radius ~1.34 Å) substitutes for the larger Ba^{2+} (1.61 Å). Such contraction is expected and supports the assumption that cerium solute is well-incorporated as Ce^{3+} onto barium sites in the lattice, rather than forming small amounts (bellow the XRD detection limit) of secondary phases by segregation or than integrating as Ce^{4+} onto titanium sites, which should determine the increase of the unit cell volume, taking into account the higher ionic radius of Ce^{4+} (0.87 Å) with respect to that of Ti^{4+} (0.605 Å).

The lack of peaks corresponding to secondary phases demonstrates that the electroneutrality condition is obeyed. This proves that the starting formula, stipulating the presence of tetra-ionized Ti vacancies (V_{Ti}'''') to compensate the effective positive extra-charge of four Ce^{3+} (4 $Ce_{Ba}^{\bullet}$) ions with respect to that of the host Ba^{2+} ions, is the valid one. These microstructural characteristics are ideal for applications requiring good ferroelectric, dielectric, or sensor behavior, particularly if a high degree of structural integrity and phase purity is needed.

The uniformity and high-quality of the annealed $Ba_{0.95}Ce_{0.05}Ti_{0.9875}O_3$ thin film at 700°C for 1 hour can be observed in the FE-SEM images of Fig. 22.

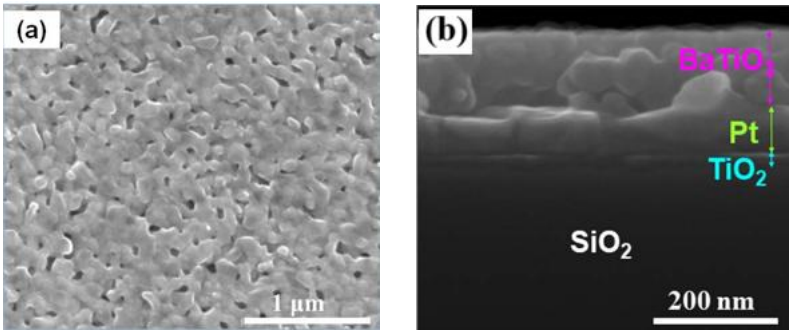


Fig. 22. (a) FE-SEM images of the surface of the BST thin film deposited on $Si/SiO_2/TiO_2/Pt$ substrate and calcined at 700°C for 1 hour, in air; (b) a cross-section detail for the $Si/SiO_2/TiO_2/Pt/BCT$ heterostructure showing its component layers [61].

The FE-SEM image of the surface reveals the presence of evenly-sized, both slightly elongated and equiaxed small grains (Fig. 22(a)). The surface is also uniform, free of cracks, exhibiting a dense microstructure. A detailed SEM image shows that the cross-section microstructure is homogeneous and dense, indicating a polycrystalline growth mechanism of "layer-by-layer" type, specific for sol-gel deposits as presented in Fig. 22(b). This observation is in good agreement with the XRD results. The estimated thickness based on the measurements on the cross-section FE-SEM images (Fig. 22(b)) of the BCT film is approximately 140 nm.

Optical properties of the BCT thin film

$BaTiO_3$ has a band gap energy of approximately 3.2 eV and does not support low-energy excitons. As a result, it serves as an optical dielectric with a moderately refractive index of around 2.5 and minimal optical losses at visible and near-infrared wavelengths [15]. This material is well-suited for use in photonic waveguides due to its low optical losses, as well as in resonant nanostructures, such as photonic metasurfaces, photonic crystals, and other nanostructures, because of its significant refractive index contrast compared to substrates like quartz. The Tauc-Lorentz model is applied for the Ce^{3+} doped BTO thin film.

The optical constants (n, k), obtained from the fitting (between experimental and simulated data), are shown in Fig. 23. It is known that the optical constants of thin films vary with the degree of crystallization, uniformity, and size of crystallites,number of structural defects, and film surface roughness.

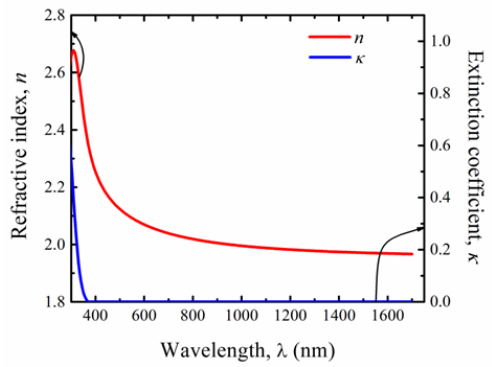


Fig. 23. The variation of optical properties *vs.* wavelength, λ, for the sol-gel BCT thin film: refraction index n and extinction coefficient k [61].

As can be seen in Fig. 23, the refractive index n decreases up to $n = 1.9$ as the wavelength increases up to $\lambda = 1700$ nm, while the extinction coefficient k drops sharply to values close to zero at wavelengths of ~ 400 nm, for BCT thin films. This can be attributed to the increasing number of thermal treatments as new layers are deposited, combined with the fact that the new layer develops on a more "orderly" previous layer. In addition, it can be seen that Ce doping leads to the increase in the refractive index of the film, the value becoming constant above the wavelength of 1100 nm. A high refractive index causes the $Ba_{0.95}Ce_{0.05}Ti_{0.9875}O_3$ (BCT) thin film to be viable for anti-reflection coatings [62].

Electrical properties of BCT thin film

The frequency dependence of both the real part of the permittivity is shown in Fig. 24(a). The real part of permittivity (ε') is almost frequency-invariant for temperatures below 300 K in the frequency range $10^3 – 10^5$ Hz. At frequency values above 10^5 Hz (*i.e.* $10^5 – 10^6$ Hz), a decrease of ε' was recorded, which is a usual feature of the $\varepsilon'(f)$ variation (Fig. 24(a)). This decrease becomes increasingly steeper as the temperature increases above 350 K for both frequency ranges, which determines a sort of

convergence of ε' when frequency approaches 1 MHz. This drop with increasing temperature can be explained in terms of thermal activated phenomena (ionic conductivity and Maxwell-Wagner phenomena associated with interfacial polarization due to a large number of grain boundary regions). The real part of permittivity shows the highest values in the low frequency region (around 10^3 Hz). At 1 kHz these values are ranging between 90 – 200 for temperatures ranged between 25 – 450 K, so that at RT, ε' exhibits a value of 150, usually recorded for doped $BaTiO_3$ thin films [61].

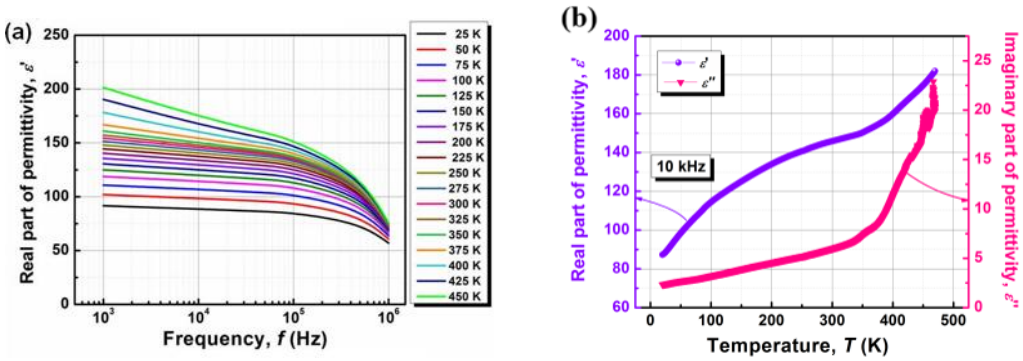


Fig. 24. (a) Frequency dependence of the real part of permittivity, ε'; (b) Temperature dependence of the real and imaginary parts of the permittivity recorded at 10 kHz for the sol-gel BCT thin film.

The temperature dependence of the real and imaginary part of the permittivity recorded at 10 kHz is shown in Fig. 24(b). Unlike the BCT bulk ceramics of similar composition, where 5 at. % Ce determines the shift of the Curie temperature and of the related permittivity maximum at room temperature, in the case of the BCT film with a thickness of only 140 nm, the temperature dependence of permittivity is so flattened that it can no longer be discussed in terms of the ferroelectric-paraelectric phase transition. This variation is specific to highly strained two-dimensional nanostructured systems and is assumed to be caused by factors such as fine graining, which strongly affects ferroelectricity, as well as the strong influence of the substrate in the case of a reduced film thickness [59, 63,64]. It is worth to mention that, at temperature values above 350 K, even this very broad temperature dependence of the real part of permittivity is hidden by the thermal activated phenomena induced by the presence of defects such as oxygen vacancies or compositional gradients in the grain boundary regions.

As for the imaginary part of the permittivity ($\varepsilon'' = \varepsilon' \cdot \tan\delta$) it exhibits quite low values, for this BCT thin film, these values being rather specific to bulk ceramics. The lowest values of ε'' are recorded in the temperature range of 25 – 425 K. At temperatures above 425 K, the much steeper increase of ε'' is related to the thermal activated phenomena already mentioned (Fig. 24(b)).

The value of the real part of permittivity of $\varepsilon' = 150$ and the low dielectric losses, $\tan\delta < 5\%$ at room temperature over a wide frequency range of $10^3 – 10^5$ Hz, together with the high thermal stability of the dielectric response, make this BCT product suitable for microwave applications.

🕮 *References*

[1] M.E. Lines, A.M. Glass, Principles and applications of ferroelectrics and related materials. Oxford: Clarendon; 1977.

[2] G.H. Haertling Ferroelectric ceramics: history and technology. J. Am. Ceram. Soc. 82 **[**4] (1999) 797-818.

[3] D. Gulwade, Lead-Free Ferroelectrics: Barium Titanate Based Ceramics: Past, Present, and Future. In: Swain, B.P. (eds) Advances in Nanostructured Materials. Materials Horizons: From Nature to Nanomaterials. Springer, Singapore, 2022.

[4] J.G. Bell, T. Graule, M. Stuer, Barium titanate-based thermistors: Past achievements, state of the art, and future perspectives. Appl. Phys. Rev. 8 (2021) 031318.

[5] T. Tsurumi, T. Hoshina, H. Takeda, Y. Mizuno, H. Chazono, Size Effect of Barium Titanate and Computer-Aided Design of Multilayered Ceramic Capacitors. IEEE Trans. Ultrason. Ferroelectrics Freq. Contr. 56 [8] (2009) 1513-1522.

[6] Z. Tian, X. Wang, L. Shu, T. Wang, T. H. Song, Z. Gui, L. Li, Preparation of Nano $BaTiO_3$-Based Ceramics for Multilayer Ceramic Capacitor Application by Chemical Coating Method. J. Am. Ceram. Soc. 92 [4] (2009) 830-833.

[7] C.A. Randall, Scientific and Engineering Issues of the State-of-the-Art and Future Multilayer Capacitors. J. Ceram. Soc. Jpn. 109 (2001) S2-S6.

[8] M.J. Pan, C.A. Randall, A brief introduction to ceramic capacitors. IEEE Electr. Insul. Mag. 26 [3] (2010) 44-50.

[9] Y. Saito, H. Takao, T. Tani, T. Nonoyama, K. Takatori, T. Homma, T. Nagaya, M. Nakamura, Lead-free piezoceramics. Nature 432 (2004) 84-87.

[10] J. Rödel, W. Jo, K. T. P. Seifert, E.-M. Anton, T. Granzow, D. Damjanovic, Perspective on the development of lead-free piezoceramics. J. Am. Ceram. Soc. 92 [6] (2009) 1153–1177.

[11] C. Deng, Y. Zhang, D. Yang, H. Zhang, M. Zhu, Recent Progress on Barium Titanate-Based Ferroelectrics for Sensor Applications. Adv. Sensor Res. 3 [6] (2024), 2300168.

[12] J.S. Capurso, A.A. Bologna, W.A. Schulze, Processing of laminated $BaTiO_3$ structures for stress-sensing applications. J. Am. Ceram. Soc.78 [9] (1995) 2476-2480.

[13] D. Shu, E. Popov, A.-L. Fehrembach, Electro-optic effect in $BaTiO_3$ for spectral tuning of narrowband resonances. J. Opt. Soc. Am. B 30 [3] (2013) 559-567.

[14] C. Xiong, W. H. P. Pernice, J. H. Ngai, J. W. Reiner, D. Kumah, F. J. Walker, Ch. H. Ahn, H. X. Tang, Active Silicon Integrated Nanophotonics: Ferroelectric $BaTiO_3$ Devices. Nano Lett. 14 [3] (2014) 1419-1425.

[15] A. Karvounis, F. Timpu, V.V. Vogler-Neuling, R. Savo, R. Grange, Barium Titanate Nanostructures and Thin Films for Photonics. Adv. Optical Mater. 8 [24] (2020), 2001249.

[16] A. M Feteira, D.C. Sinclair, I.M. Reaney, Y. Somiya, M. Lanagan, BaTiO3-Based Ceramics for Tunable Microwave Applications. J. Am. Ceram. Soc. 87 [6] (2004) 1082-1087.

[17] Z. Xiong, Q. Liu, J. Tang, L. Fang, X. Zhang, J. Li, Y. Fu, J. Wang, Z. Gao, A wide-frequency range dielectric tuning of $BaTiO_3$ by embedding metal nanocrystals, RSC Adv**.** 11 [24] (2021) 14578–14586.

[18] A. Ianculescu, Z.V. Mocanu, L.P. Curecheriu, L. Mitoseriu, L. Padurariu, R. Trusca¸ Dielectric and tunability properties of La-doped $BaTiO_3$ ceramics, J. Alloy Compd, 509 [41] (2011), 10040–10049.

[19] A. Jain, Y.G. Wang, L.N. Shi, Recent developments in $BaTiO_3$ based lead-free materials for energy storage applications. J. Alloys Compd. 928 (2022), 167066.

[20] M. Zhou, R. Liang, Z. Zhou, X. Dong, Novel $BaTiO_3$-based lead-free ceramic capacitors featuring high energy storage density, high power density, and excellent stability. J. Mater. Chem. C 6 [31] (2018) 8528–8537.

[21] Y. Li, M.-Y. Tang, Z.-G. Zhang, Q. Li, J.-L. Li, $BaTiO_3$-based ceramics with high energy storage density. Rare Met. 42 [4] (2023) 1261–1273.

[22] Y.B. Adediji, A.M. Adeyinka, D.I. Yahya, A review of energy storage applications of lead-free $BaTiO_3$-based dielectric ceramic capacitors. Energy Ecol. Environ. 8 [5] (2023) 401–419.

[23] K. Tagantsev, V.O. Sherman, K.F. Astafiev, J. Venkatesh, N. Setter, Ferroelectric materials for microwave tunable applications. J. Electroceram. 11 [1-2] (2003) 5–66.

[24] O.G. Vendik, Dielectric nonlinearity of the displacive ferroelectrics at UHF. Ferroelectrics 12 [1] (1976) 85–90.

[25] **E.M. Soare, C.A. Stanciu, R.E. Pătru, V.A. Surdu, N. Horchidan, L. Mitoșeriu, I. Pintilie, B.Ș. Vasile, A.I. Nicoară, R.D. Truşcă, A.C. Ianculescu, Composition-dependent structural, microstructural and functional characteristics of fine-grained $BaTi_{1-x}Hf_xO_3$ ceramics consolidated by Spark Plasma Sintering. J. Eur. Ceram. Soc. 45 (2025) 117600**

[26] **R.E. Pătru, C.A. Stanciu, V.A. Surdu, E.M. Soare, R.D. Truşcă, B.S. Vasile, A.I. Nicoară, L. Trupină, I. Pasuk, M. Botea, N. Horchidan, L. Mitoşeriu, L. Pintilie, I. Pintilie, A.C. Ianculescu, Downscaling grain size toward the nanometre range - a key-factor for tuning the crystalline structure, phase transitions, dielectric and ferroelectric behaviour in $Ba_{0.8}Sr_{0.2}TiO_3$ ceramics. Prog. Solid State Chem. 74 (2024) 100457.**

[27] T. Takeuchi, K. Ado, T. Asai, H. Kageyama, Y. Saito, C. Masquelier, O. Nakamura, Thickness of Cubic Surface Phase on Barium Titanate Single-Crystalline Grains. J. Am. Ceram. Soc. 77 [6] (1994) 1665–1668

[28] M.B. Smith, K. Page, Th. Siegrist, P.L. Redmond, E.C. Walter, R. Seshadri, L.E. Brus, M.L. Steigerwald. Crystal Structure and the Paraelectric-to-Ferroelectric Phase Transition of Nanoscale $BaTiO_3$. J. Am. Chem. Soc. 130 [22] (2008) 6955–6963.

[29] V. Petkov, V. Buscaglia, M.T. Buscaglia, Z. Zhao, Y. Ren. Structural coherence and ferroelectricity decay in submicron- and nano-sized perovskites. Phys. Rev. B 78 [5] (2008) 054107.

[30] K. Page, T. Proffen, M. Niederberger, R. Seshadri, Probing Local Dipoles and Ligand Structure in $BaTiO_3$ Nanoparticles. Chem. Mater. 22 [15] (2010) 4386–4391.

[31] Y. Gao, V.V. Shvartsman, D. Gautam, M. Winterer, D.C. Lupascu. Nanocrystalline Barium Strontium Titanate Ceramics Synthesized via the "Organosol" Route and Spark Plasma Sintering. J. Am. Ceram. Soc. 97 [7] (2014) 2139–2146.

[32] M. Botea, I. Pintilie, V.A. Surdu, C.A. Stanciu, R.D. Truşcă, B. S. Vasile, R. Patru, A.C. Ianculescu, L. Pintilie. Structural, functional properties and enhanced thermal stability of bulk graded (Ba, Sr)TiO_3 structures obtained by spark plasma sintering. J. Mater. Res. Technol. 12 (2021) 2085–2103.

[33] K. Uchino, S. Nomura, Critical Exponents of the Dielectric Constants in Diffused-Phase-Transition Crystals. Ferroelectrics – Lett. Section 44 [1] (1982) 55–61.

[34] J. Li, D. Zhang, S. Qin, T. Li, M. Wu, D. Wang, Y. Bai, X. Lou. Large room-temperature electrocaloric effect in lead-free $BaHf_xTi_{1-x}O_3$ ceramics under low electric field, Acta Mater. 115 (2016) 58–67.

[35] M.D. Li, X.G. Tang, S.M. Zeng, Q.X. Liu, Y.P. Jiang, T.F. Zhang, W.H. Li, Large Electrocaloric Effect in Lead-free $Ba(Hf_xTi_{1-x})O_3$ Ferroelectric Ceramics for Clean Energy Applications. ACS Sustain. Chem. Eng. 6 [7] (2018) 8920–8925.

[36] M.D. Li, X.G. Tang, S.M. Zeng, Q.X. Liu, Y.P. Jiang, T.F. Zhang, W.H. Li, Phase structure analysis and pyroelectric energy harvesting performance of $Ba(Hf_xTi_{1-x})O_3$ ceramics. J. Am. Ceram. Soc. 102 [6] (2019) 3623-3629.

[37] S. Anwar, P.R. Sagdeo, N.P. Lalla, Crossover from classical to relaxor ferroelectrics in $BaTi_{1-x}Hf_xO_3$ ceramics. J. Phys. Condens. Matter. 18 [13] (2006) 3455–3468.

[38] S. Anwar, P.R. Sagdeo, N.P. Lalla, Study of the relaxor behaviour in $BaTi_{1-x}Hf_xO_3$ ($0.20 \leq x \leq 0.30$) ceramics. Solid State Sci. 9 [11] (2007) 1054–1060.

[39] S. Anwar, P.R. Sagdeo, N.P. Lalla, Locating the normal to relaxor phase boundary in $Ba(Ti_{1-x}Hf_x)O_3$ ceramics. Mater. Res. Bull. 43 [7] (2008) 1761–1769.

[40] H.Y. Tian, Y. Wang, J. Miao, H.L.W. Chan, C.L. Choy, Preparation and characterization of hafnium-doped barium titanate ceramics. J. Alloy Compd. 431 [1-2] (2007) 197–202.

[41] W.H. Payne, V.J. Tennery, Dielectric and Structural Investigations of the System $BaTiO_3$-$BaHfO_3$. J. Am. Ceram. Soc. 48 [8] (1965) 413–417.
[42] J. Fernandez, B. Bindhu, M. Prabu, K. Y. Sandhya, Effects of hafnium on the structural, optical and ferroelectric properties of sol-gel synthesized barium titanate ceramics. J. Korean Ceram. Soc. 59 (2022) 240–251.
[43] P. Elorika, Sh. Anwar, S. Anwar, Impact of synthesis-induced disorder on the structural, electrical, and optical properties of $BaTi_{1-x}Hf_xO_3$, $0 \leq x \leq 0.08$. Mater. Res. Bull. 167 (2023) 112424.
[44] S.K. Das, B.K Roul, Double hysteresis loop in $BaTi_{1-x}Hf_xO_3$ ferroelectric ceramics. J. Mater. Sci: Mater. Electron. 26 [8] (2015) 5833-5838
[45] H.M. Yin, W.J. Xu, H.W. Zhou, X.Y. Zhao, Y.N. Huang, Effects of phase composition and grain size on the piezoelectric properties of HfO2-doped barium titanate ceramics. J. Mater. Sci. 54 [19] (2019) 12392-12400.
[46] Z. Zhao, V. Buscaglia, M. Viviani, M.T. Buscaglia, L. Mitoseriu, A. Testino, M. Nygren, M. Johnsson, P. Nanni, Grain-size effects on the ferroelectric behavior of dense nanocrystalline $BaTiO_3$ ceramics. Phys. Rev. B. 70 (2004) 024107.
[47] M.T. Buscaglia, M. Viviani, V. Buscaglia, L. Mitoseriu, A. Testino, P. Nanni, Z. Zhao, M. Nygren, C. Harnagea, D. Piazza, C. Galassi, High dielectric constant and frozen macroscopic polarization in dense nanocrystalline $BaTiO_3$ ceramics. Phys. Rev. B 73 (2006) 064114.
[48] V. Buscaglia, C.A. Randall, Size and scaling effects in barium titanate. An overview, J. Eur. Ceram. Soc. 40 (2020) 3744-3758.
[49] V.L. Ene, V.R. Lupu, C.V. Condor, R. E. Patru, L. M. Hrib, L. Amarande, A. I. Nicoara, L. Pintilie, A.C. Ianculescu, Influence of Grain Size on Dielectric Behavior in Lead-Free $0.5Ba(Zr_{0.2}Ti_{0.8})O_3$-$0.5(Ba_{0.7}Ca_{0.3})TiO_3$ Ceramics. Nanomaterials, 13 (2023) 2934.
[50] L. Curecheriu, S.B. Balmus, M.T. Buscaglia, V. Buscaglia, A. Ianculescu, L. Mitoseriu, Grain Size-Dependent Properties of Dense Nanocrystalline Barium Titanate Ceramics. J. Am. Ceram. Soc. 95 (2012) 3912–3921.
[51] **R.E. Pătru, C.A. Stanciu, E.M. Soare, V.A. Surdu, R.D. Truşcă, A.I. Nicoară, B.S. Vasile, G. Boni, L. Amarande, N. Horchidan, L.P. Curecheriu, L. Mitoşeriu, L. Pintilie, I. Pintilie, A.C. Ianculescu, Grain size-driven effect on the functional properties in $Ba_{0.6}Sr_{0.4}TiO_3$ ceramics consolidated by spark plasma sintering. J. Eur. Ceram. Soc. 43 (2023) 3250–3265.**
[52] **E.M. Soare, C.A. Stanciu, R.E. Pătru, V.A. Surdu, L. Pădurariu, N. Horchidan, A.I. Nicoară, L. Trupină, B.Ș. Vasile, R.D. Truşcă, L. Mitoșeriu, A.C. Ianculescu, Grain size effects in $BaTi_{0.90}Hf_{0.10}O_3$ ceramics with phase coexistence: the influence of nanostructuring and of the internal stress on the functional properties. J. Mater. Res. Technol**. **https://doi.org/10.1016/j.jmrt.2025.08.195**
[53] A.J. Bell, L.E. Cross, A phenomenological Gibbs function for BaTiO3 giving correct E-field dependence of all ferroelectric phase changes. Ferroelectrics 59 (1984) 197–203.
[54] A.J. Bell, Phenomenologically derived electric field-temperature phase diagrams and piezoelectric coefficients for single crystal barium titanate under fields along different axes. J. Appl. Phys. 89 (2001) 3907-3914.
[55] Z. Yu, C. Ang, R. Guo, A.S. Bhalla, Piezoelectric and strain properties of $BaTi_{1-x}Zr_xO_3$ ceramics. J. Appl. Phys. 92 [3] (2002) 1489–1493
[56] S.P. Yordanov, I. Ivanov, C. P. Carapanov, Dielectric properties of the ferroelectric Bi2Ti2O7 ceramics. J. Phys. D. 31 [7] (1998) 800–806.
[57] L.E. Cross, Relaxor ferroelectrics: An overview. Ferroelectrics 151 (1994) 305–320.
[58] K. Uchino, Ferroelectric Devices. New York: Marcel Dekker Inc.; 2000.
[59] A. Ianculescu, B. Despax, V. Bley, T. Lebey, R. Gavrilă, N. Drăgan, Structure–properties correlations for barium titanate thin films obtained by rf-sputtering, J. Eur. Ceram. Soc. 27 [2] (2007) 1129–1135.
[60] S. Yasmin, S. Choudhury, M. A. Hakim, A. H. Bhuiyan, M. J. Rahman, Structural and dielectric properties of pure and cerium-doped barium titanate. J. Ceram. Process. Res. 12 [4] (2011) 387–391.

[61] **E.M. Soare, R. Truşcă, M. Anastasescu, A. Ianculescu, M. Gartner, C.A. Stanciu, Structural and optical characterization of Ce-doped $BaTiO_3$ thin films prepared by the sol-gel method, accepted for publication in U.P.B. Sci. Bull. Series B (2025).**

[62] Y. Iriani, A. Suparmi, A. Marzuki, D.K. Sandi, Microstructures and Optical Properties of Nanocrystalline Pr- doped $BaTiO_3$ Thin Film. Int. J. Thin.Film. Sci. Tec. 11 [3] (2022) 307–311.

[63] C.A. Stanciu, I. Pintilie, A.V. Surdu, R. Truşcă, B.S. Vasile, M.A. Eftimie, A.C. Ianculescu, Influence of sintering strategy on the characteristics of sol-gel $Ba_{1-x}Ce_xTi_{1-x/4}O_3$ ceramics. Nanomaterials. 9 [12] (2019) 167.

[64] N.A. Pertsev, A.G. Zembilgotov, A.K. Tagantsev, Effect of Mechanical Boundary Conditions on Phase Diagrams of Epitaxial Ferroelectric Thin Films. Phys. Rev. Lett. 80 [9] (1998) 1988–1991.